

Design and Implementation of Evanescent Mode Waveguide Filters Using Dielectrics and Additive Manufacturing Techniques

Alejandro Pons-Abenza, *Student Member, IEEE*, José-María García-Barceló, Antonio Romera-Pérez, Alejandro Alvarez-Melcon, *Senior Member, IEEE*, Fernando Quesada-Pereira, *Member, IEEE*, Juan Hinojosa-Jiménez, *Senior Member, IEEE*, Marco Guglielmi, *Fellow, IEEE*, Vicente Boria, *Fellow, IEEE*, and Lara Arche-Andradas,

Abstract—In this contribution, we describe the design of bandpass filters using evanescent mode waveguides and dielectric resonators implemented with additive manufacturing techniques. Two C-band Chebyshev evanescent mode waveguide filters of order five have been designed using a low cost commercial dielectric material (ABSplus), widely used by Fused Deposition Modeling (FDM) 3D printers. The housings of the filters have been manufactured using traditional computer numerical control (CNC) machining techniques. Practical manufacturing considerations are also discussed, including the integration of dielectric and metallic parts. We first discuss two breadboards using two different resonator geometries. We then demonstrate how different transfer functions can be easily implemented by changing the 3D printed parts in the same metallic housing. Breadboards show fractional bandwidths between 3% and 4.6% with return losses better than $RL = 18$ dB, and spurious free ranges of $SFR = 1$ GHz. Insertion losses are better than $IL = 4.3$ dB. Even though dielectric losses from the plastic material are shown to be high, the measured results are quite satisfactory, thereby clearly showing that this strategy maybe useful for the fast production of low cost microwave filters implementing complex geometries.

Index Terms—3D-printers, ABSplus, additive manufacturing, dielectric resonators, evanescent mode waveguides, microwave filters, selective laser melting.

I. INTRODUCTION

THE design of filters in waveguide technology remains one of the most important activities in the microwave engineering field [1]. Waveguide filters are, in fact, used in the input/output stages of many systems, for both space and ground application, where low loss and high-power handling are critical requirements [2]. In addition, physical constraints such as low volume and small footprint are usually required.

Manuscript received xx xx, 2019; revised xx xx, xxxx.

This work is supported in part by Thales Alenia Space (Tres Cantos, Madrid, Spain), and by the grant TEC2016-75934-C4-4-R in collaboration with TEC2016-75934-C4-1-R of MEC, Spain.

A. Pons, J.M. García, A. Romera, A. Álvarez, F. Quesada are with Department of Information and Communication Technologies (DTIC), Electromagnetism Applied to Telecommunications research group (GEAT) at Technical University of Cartagena (Murcia, Spain).

J. Hinojosa is with Department of Electronics, Projects and Computer Technologies at Technical University of Cartagena (Murcia, Spain).

M. Guglielmi and V. Boria are with ITEAM (Instituto de Telecomunicaciones y Aplicaciones Multimedia) at Technical University of Valencia (Valencia, Spain).

L. Arche is with Thales Alenia Space Spain (Tres Cantos, Madrid, Spain).

Furthermore, the most common implementation of microwave waveguide filters is based on CNC machining of aluminum. Unfortunately, however, CNC machining techniques have limitations in terms of manufacturing certain complex geometries [3].

In this context, therefore, emerging Additive Manufacturing (AM) techniques are becoming very attractive to produce novel passive filter geometries and microwave devices [4], [5]. Using AM techniques complex shapes can, in fact, be very easily manufactured [6]. Using thermoplastic as base material, for instance, and using subsequent metallization of the hardware, one can dramatically reduce the overall mass of the filter structure [7]. In [8] the metallization of the walls is achieved using an automated deposition process of conductive silver ink. A similar, although more elaborated strategy is used in [9], where air channels are implemented into the walls of the plastic pieces, which are then filled with a liquid metal. It is also interesting to remark that a similar concept was used in [8] to build a waveguide switch. In this case the switch operation is achieved by pumping in and out the liquid metal through plastic tubes. Additionally, smart optimization of the shape of traditional implementations can significantly reduce the Insertion Losses (IL) of the filters [10]. Other authors have tried direct geometrical modifications on the cavity resonator itself, using curvilinear shapes, leading to new resonators with significant improvements in terms of unloaded quality factors (Q_U). Interesting works in this direction are the spherical resonators proposed in [11], [12], or the use of complex curvilinear shapes as proposed in [13].

The implementation of dielectric resonators has also been recently explored in the context of AM. A list of thermoplastics and ceramics showing good dielectric properties can, in fact, be found for many FDM or Stereo-lithography (SLA) commercial 3D-printers [14], [15]. Various strategies have also been discussed to incorporate AM dielectrics into a waveguide filter structure. An interesting example can be found in [16], where a TM-mode dielectric resonator based on alumina with $\tan \delta < 0.002$ and $\epsilon_r \approx 9.9$ is used to directly print a second order filter. After the hardware has been printed, the external faces are metallized to build the lateral walls of the structure. The filter shows good performance in terms of losses, but with slight frequency deviations due to the lack of accuracy of the AM process. An alternative solution is to design the dielectric

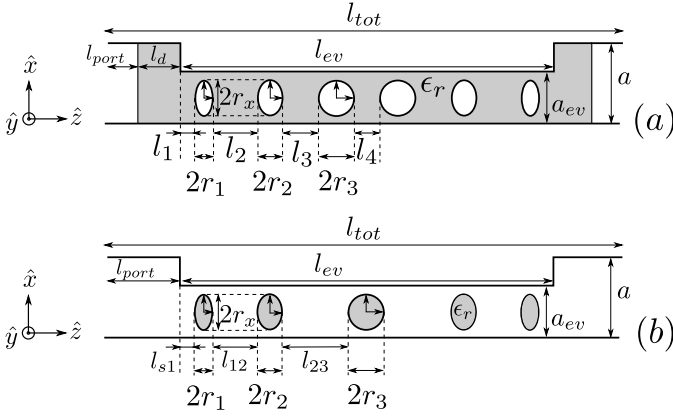


Fig. 1. 2D sketches of the evanescent mode filters proposed in this paper. (a) Design with air holes inside a dielectric block filling a waveguide section with reduced width (air-holes filter). (b) Design with dielectric posts inside an otherwise empty evanescent waveguide section (ϵ_r -posts filter).

resonators from a single piece of plastic, which is then fastened in the filter using the metallic parts of the coupling windows. This strategy is demonstrated in [17], where the dielectric resonators are printed from a single plastic bar, following an in-line topology, or in [18], where a more complex connection mechanism between resonators is proposed.

In this context therefore, we contribute to the state-of-the-art of AM manufacturing of waveguide filters by showing how the two evanescent mode filter designs shown in Fig. 1 can be manufactured using 3D printing techniques. The objective of this paper is to compare two different solutions for evanescent mode filters that can be rapidly and inexpensively manufactured with 3D-printing using commercial AM dielectric materials. The filter structures discussed in this paper combine AM parts for the dielectric elements, with conventional aluminum CNC machining, thus leading to a hybrid manufacturing strategy. Following this strategy, the metallic parts of the structure are kept simple, while complex geometries may be easily manufactured for the dielectric elements.

The dielectric elements proposed in this work are implemented with a low cost commercial ABSplus plastic from Stratasys, with relative dielectric constant $\epsilon_r = 3.55$ [19]. This material has recently become widely available in low cost 3D printers. The first solution, shown in Fig. 1(a), consists of a filter with a reduced width, dielectric-filled rectangular waveguide, where inter resonator couplings are implemented with elliptical air holes (subsequently referred to as the air-hole filter). The complementary approach is followed in the second design, where several elliptic dielectric post resonators are placed inside an empty evanescent rectangular waveguide section, as shown in Fig. 1(b) (subsequently referred to as the ϵ_r -post filter).

The two structures proposed in this work have been manufactured with a hybrid strategy. Namely, the 3D printed plastic pieces have been manufactured using an FDM 3D printer, while the aluminum housings have been manufactured using standard CNC machining. This strategy allows for a fast and low cost implementation of the filters, although at the expense of somewhat higher insertion losses. An additional benefit

of this hybrid manufacturing strategy is also demonstrated in this paper. Namely, several filters with different transfer functions can be easily implemented using the same external aluminum housing. What is needed is just the design of new dielectric parts, which are then manufactured with the 3D printer. Following this approach, only one *common* external housing is manufactured with CNC machining techniques, while high flexibility can be obtained by producing several low cost plastic pieces to implement different transfer functions.

Overall, the measured performance of the manufactured prototypes is good, thereby fully confirming the practical feasibility of the new concepts proposed in the paper.

II. FILTERS DESIGN

The filters used in this work to demonstrate the hybrid manufacturing strategy are two 5-pole Chebyshev filters with 20 dB return loss (RL). The filters have been designed at C-band with a center frequency $f_c = 3.68$ GHz and a bandwidth $BW = 120$ MHz (fractional bandwidth $FBW \approx 3.2\%$). The filters are designed using an in-line topology, since no cross-couplings will be considered for simplicity. It is important to note, however, that cross coupled structures can also be easily implemented. The coupling matrix, which is the same for both filters, has all elements equal to zero, except for couplings along the in-line channel ($M_{i,i+1}$) [2]

$$\begin{aligned} M_{S1} = M_{5L} = 1.0137, \quad M_{12} = M_{45} = 0.8653, \\ M_{23} = M_{34} = 0.6357. \end{aligned} \quad (1)$$

2D sketches of the proposed filters are presented in Fig. 1. A standard WR-229 waveguide has been used for the input/output waveguide ports ($a = 58.17$ mm, $b = 29.083$ mm). The first filter, shown in Fig. 1(a), consists of a dielectric piece placed inside a reduced width waveguide section, with a series of air holes. This filter uses the fundamental TE_{10} mode, which can propagate in the dielectric filled waveguide section, while the air holes, where the fundamental mode is below cut-off, are used to implement the coupling elements between resonators. The width of the waveguide section is reduced to avoid the propagation of higher order modes, when it is filled with the dielectric material. The physical separation between air holes [l_i in Fig. 1(a)] controls the resonant frequency of each resonator. The air holes are implemented as elliptical cylinders, and their dimensions [r_i according to Fig. 1(a)] are used to control the coupling level between adjacent resonators. Consequently, for the design of our 5th-order filter, a total of six air holes are required. With this arrangement, the input/output couplings are controlled with the sizes of the first and last air holes. However, the step discontinuity needed for implementing the reduced width waveguide section will also affect this coupling.

As it can be observed in Fig. 1(a), the dielectric piece is longer than the waveguide section (l_{ev}). The extra length (l_d) will facilitate the alignment of the dielectric piece with the external metallic housing. We also verified that this extra dielectric section helps to increase the input/output coupling levels of the filter. However, the extra length (l_d) cannot be very large, as this area may become resonant due the formation

of an air-dielectric discontinuity. As it will be shown later in this paper, this suggests that, in practice, a trade-off is needed to adjust the length l_d .

The second solution proposed in this paper is shown in Fig. 1(b). In this case, instead of filling the whole waveguide with a dielectric material, only several cylindrical dielectric posts are placed inside an empty waveguide section. With this arrangement the fundamental TE₁₀ mode is below cut-off in the evanescent waveguide section, and the dielectric posts become resonant. Consequently, the dimensions of these posts [r_i according to Fig. 1(b)] control the resonant frequency of each resonator, while the physical distances between adjacent posts [$l_{i,i+1}$ in Fig. 1(b)] control the coupling level by proximity. For our 5th-order filter, a total of 5 dielectric posts are required. Intuitively, this solution may be more compact, since less posts (as compared to air-holes) are required to implement the same frequency response. For this solution, the input/output couplings are implemented with the distance between the ports and the first (or last) dielectric resonator [l_{s1} in Fig. 1(b)]. However, the maximum coupling that can be achieved is strongly determined by the step junction needed to form the evanescent waveguide section.

It is important to note that in both structures shown in Fig. 1, the cylinders are of elliptical shape, and we have fixed the radius along the x -axis to $r_x = 14$ mm. This assures a 1 mm gap between the waveguide side walls and each post, for a width of the evanescent waveguide section of $a_{av} = 30$ mm.

For the design process, a variation of the classical even/odd analysis technique has been used [20]. This approach is based on calculating the even-odd resonant frequencies (f_e , f_o) of two symmetric coupled resonators working at the center frequency (f_c). The frequency scaled coupling coefficient can then directly be computed from these two frequencies as [2], [21]

$$k_{sc} = \frac{f_e^2 - f_o^2}{f_e^2 + f_o^2}, \quad (2)$$

and the normalized coupling coefficient, which is directly related to the coupling matrix values given in (1), can be calculated as [2], [21]

$$k_{norm} = M_{ij} = \frac{f_c}{BW} k_{sc}. \quad (3)$$

The normalized coupling values (M_{ij}), obtained for the two types of resonators we propose, are presented in Fig. 2. The same figure is employed to present the results obtained for the two configurations discussed in this paper, by using two independent vertical axes. For the configuration shown in Fig. 1(a), the coupling is given as a function of the air-hole semi-axis (r_i), while the length (l_{ij}) is used for the second configuration shown in Fig. 1(b).

The levels computed for M_{ij} are suitable in both cases to obtain the filters with the initial specifications. It can be observed that, to implement an equal coupling level, the configuration with dielectric posts will in general be smaller than the one with air-holes ($l_{ij} < r_i$). This indicates that, for equal responses, the solution with dielectric posts will result in a more compact structure.

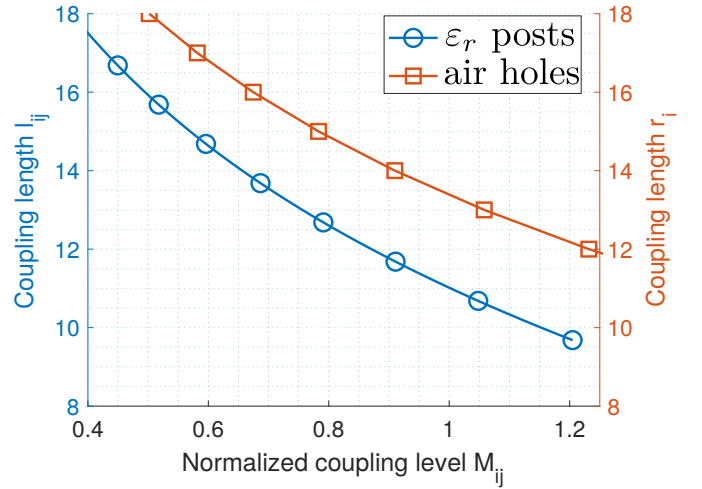


Fig. 2. Normalized inter-resonator coupling curves for the two proposed configurations. Legend refers to Fig. 1(a) (air-holes) and to Fig. 1(b) (ϵ_r -posts). For this test ($a_{ev} = 30$ mm).

It is well known that for the input/output coupling, a different procedure must be followed. This procedure consists of adjusting the external quality factor (Q_{ext}) of a single resonator to the value calculated from the coupling matrix, namely [2], [21]

$$Q_{ext} = \frac{f_c}{M_{S1}^2 BW}. \quad (4)$$

A doubly-terminated resonator structure can be used for this purpose. This will allow the computation of the Q_{ext} as a function of the physical parameter of the filter related to the input/output couplings. For our two configurations, the key parameters are the elliptical semi-axis of the first air-hole (r_1) [air-hole filter, Fig. 1(a)] and the distance to the first resonator (l_{s1}) [dielectric post filter, Fig. 1(b)]. The corresponding results for each structure are shown in Fig. 3. Similarly to Fig. 2, two different ordinate axes have been used to show both results on the same plot.

As we can see from the Q_{ext} curves shown in Fig. 3, the slopes are similar. However, the structure with dielectric posts can achieve lower Q_{ext} values. Therefore, this structure is more suitable to implement filters with wider passbands as compared to the filter with air-holes. This behavior is enhanced by the fact that the coupling distance l_{s1} in Fig. 1(b) can be made slightly negative, meaning that the first and last resonators are slightly introduced in the port section [l_{port} of Fig. 1(b)].

Another interesting conclusion can be pointed out from the plot shown in Fig. 3. For narrowband filters, where larger Q_{ext} values are needed, the filter with dielectric posts has the potential to be more compact. As shown in the plot, large Q_{ext} values require smaller coupling distances (l_{s1}) for the dielectric posts filter, as compared to the diameter ($2r_1$) of the air-holes filter ($l_{s1} < 2r_1$). For instance, to synthesize $Q_{ext} = 100$, a coupling length $l_{s1} = 16$ mm is needed, while the axis of the air-hole needs to be larger ($2r_1 = 20$ mm). This confirms the behavior already observed for the inter-resonator couplings in Fig. 2. For the same in-band response, more

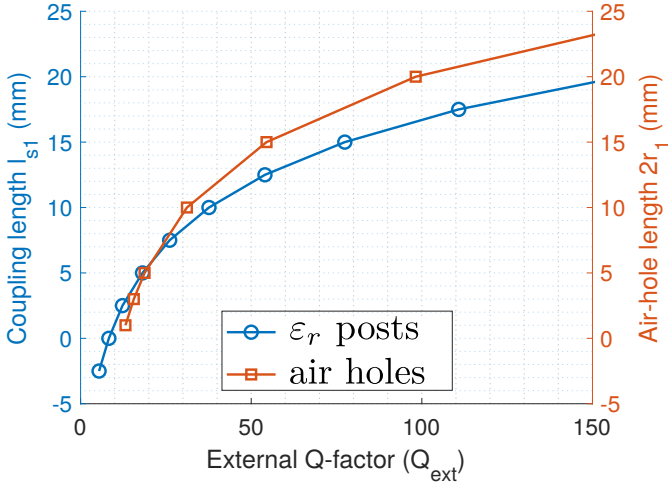


Fig. 3. External quality factor (Q_{ext}) for the two proposed evanescent filters. The legend refers to Fig. 1(a) (air-holes) and to Fig. 1(b) (ϵ_r -posts). For this test we have fixed: $a_{ev} = 30$ mm, $l_d = 7$ mm, $l_1 = 0$ mm.

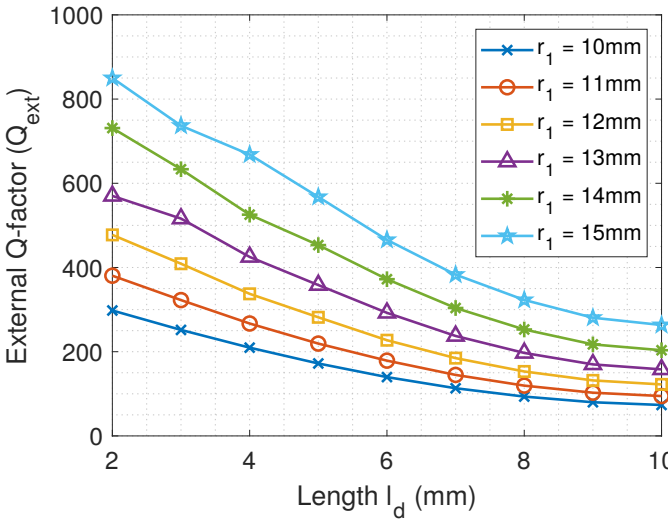


Fig. 4. Q_{ext} values for the air-holes filter as a function of the extra length (l_d), for various values of the input semi-axis (r_1). For this test we have fixed: $a_{ev} = 30$ mm, $l_1 = 0$ mm.

compact structures can be obtained with the configuration based on dielectric posts.

As already mentioned, the input coupling of the air-hole filter is also affected by the extra length (l_d) used to align the dielectric piece with the external housing. In order to study this effect, we present in Fig. 4 the Q_{ext} values for this filter as a function of the extra length (l_d) for various values of the input air-hole semi-axis (r_1). As we can see, the Q_{ext} value decreases when the length l_d is increased. This indicates that l_d can be used to increase the input coupling of the filter, if wideband responses are needed. On the other hand, the plot shows that the slope is greater when the semi-axis of the air-hole (r_1) is larger. Therefore, the sensitivity of the input coupling with the length (l_d) will be stronger for narrowband responses. The plot also indicates that the effect tends to saturate for lengths $l_d > 8$ mm. Further increase of this length does not translate in substantially higher input

TABLE I
FINAL DIMENSIONS OF THE DESIGNED AIR-HOLES FILTER ACCORDING TO FIG. 1(A).

Var.	Value (mm)	Var.	Value (mm)	Var.	Value(mm)
l_{port}	10	l_1	0	r_1	4.859
l_d	7	l_2	22.11	r_2	14.54
l_{ev}	258.847	l_3	23.23	r_3	16.86
l_{tot}	292.847	l_4	23.13	r_x	14

TABLE II
FINAL DIMENSIONS OF THE DESIGNED DIELECTRIC POSTS FILTER ACCORDING TO FIG. 1(B).

Var.	Value (mm)	Var.	Value (mm)	Var.	Value (mm)
l_{port}	15	l_{s1}	-0.439	r_1	13.619
l_{tot}	275.016	l_{12}	24.6	r_2	14.208
l_{ev}	245.016	l_{23}	28.474	r_3	14.219

coupling. In addition, we have verified that it is not convenient to take very large values for the length l_d . This is because the junction may become resonant in the area between the waveguide step and the air-dielectric discontinuity. Taking into consideration all the practical aspects discussed so far, and the behavior shown in Fig. 4, an optimum value of $l_d = 7$ mm has been selected for the designs presented in this paper.

Using the data shown in Fig. 2 and Fig. 3, the initial dimensions for the two filters can now be easily obtained. The final *optimized* filter dimensions are shown in Table I and Table II, respectively. The wide band responses for both filters are presented in Fig. 5. The results shown have been obtained with the full-wave simulator HFSS [22]. As we can see, the responses of the two filters are very similar, both inside and outside the passband. The out of band responses indicate that the spurious free ranges (SFR) of both filters are also very similar. In particular, the first spurious band appears at $f_{sp} \approx 4.8$ GHz, giving $SFR \approx 1$ GHz.

Except for the insertion losses (IL), that will be discussed in the next section, the results obtained indicate that the

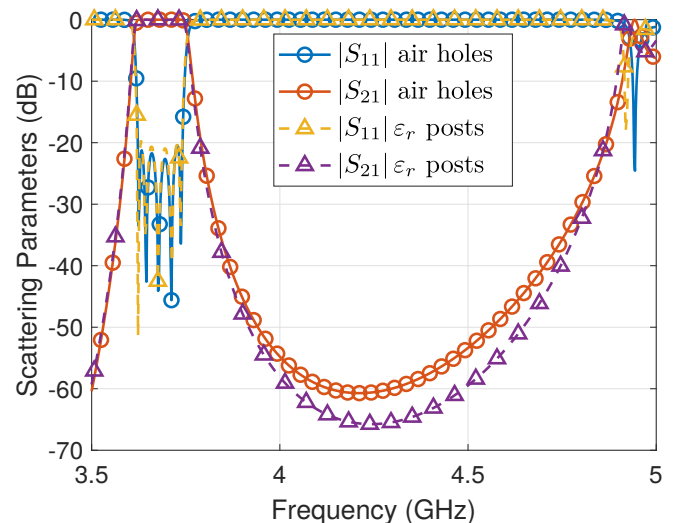


Fig. 5. Frequency responses obtained for the two designed filters. The legend refers to Fig. 1(a) (air-holes) and to Fig. 1(b) (ϵ_r -posts).

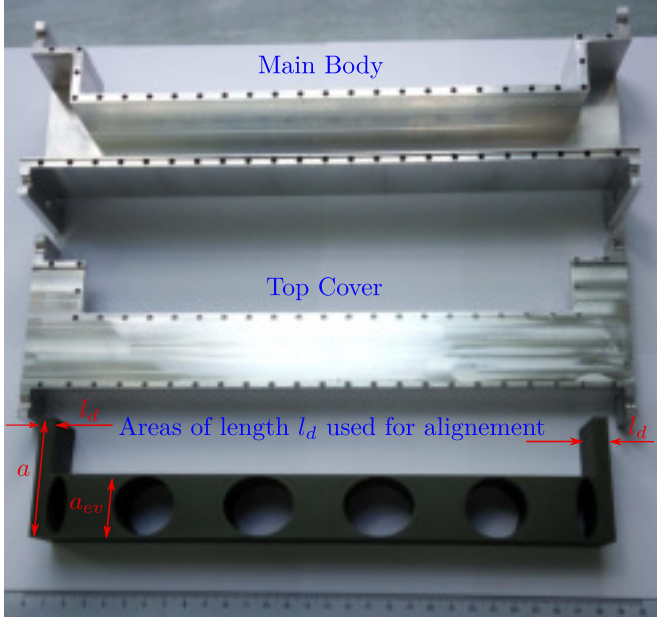


Fig. 6. Pieces of the manufactured air-holes filter, showing the two extended areas of length (l_d) used for alignment of the dielectric block inside the main body.

performance of both filters is essentially the same one, at least from the electrical point of view. Mechanically, however, there are some important differences. First, the dimensions of Table I indicate that the total length of the filter with air-holes [Fig. 1(a)] is $l_{tot} = 292.847$ mm. For the second filter [Fig. 1(b)], the data of Table II indicate a total length of $l_{tot} = 275.016$ mm. This confirms that, as previously discussed, the filter based on dielectric posts is more compact than the filter based on air-holes. This can be a convenient feature for practical applications, where reduction in footprint is important.

III. EXPERIMENTAL RESULTS

The two filters designed in the previous section have been implemented using a hybrid manufacturing approach. AM has been used for the dielectric parts, while the metallic housings have been manufactured using standard CNC milling. The metallic parts have been manufactured using aluminum, while the dielectric parts have been printed using ABSplus with a 3D-printer, model Dimension 1200-bst [23].

The pieces manufactured for the air-hole filter are shown in Fig. 6. As we can see, the housing is manufactured in two pieces, namely, a main body and a top cover. This geometry is very simple, so a standard CNC milling process can be used. The dielectric piece is manufactured with the 3D printer in one single block, including all resonators and couplings. As a result, the alignment of the dielectric piece inside the metallic body is extremely simple. The alignment is also facilitated by the use of the two extended areas of length $l_d = 7$ mm at both extremes of the piece, as shown in Fig. 6.

The measured results, directly obtained from the prototype manufactured, are shown in Fig. 7 using circle symbols. They are compared with the results obtained with HFSS

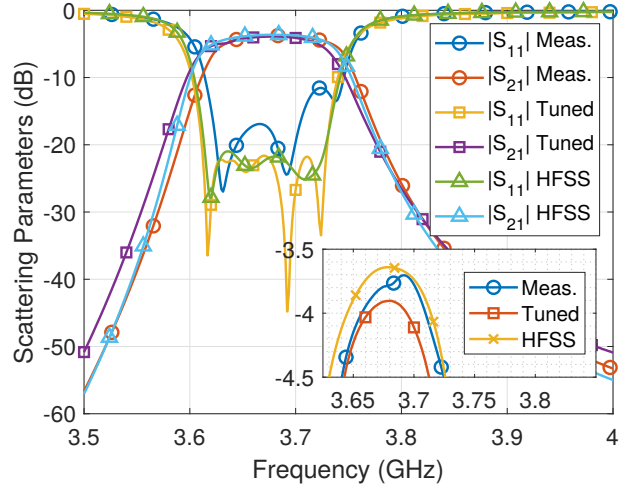


Fig. 7. S-Parameter comparison between measured results directly obtained after manufacturing (circle symbols), measured results after tuning (square symbols) and simulated results obtained with HFSS after introducing losses (triangle and cross symbols) ($\tan \delta = 0.0053$, $\sigma = 3.8 \cdot 10^7$ S/m). Inset in the figure shows details of the measured and simulated minimum insertion losses within the passband.

when losses are included in the simulations (triangle and cross symbols). As we can see, the response obtained directly after manufacturing is in reasonably good agreement with the simulations performed with HFSS including losses.

To include losses in the simulations, we have used for the ABSplus a loss tangent value equal to $\tan \delta = 0.0053$. This value corresponds to the largest value specified by the manufacturer ($0.0046 < \tan \delta < 0.0053$) [19]. In addition, for the external aluminum housing, the conductivity value used is ($\sigma = 3.8 \cdot 10^7$ S/m). However, we have verified that the losses due to the finite conductivity of the external housing have very little influence on the overall insertion loss performance of the filter. This study confirms that the important contribution of losses is due to the loss tangent of the ABSplus. As observed in the inset of Fig. 7, the minimum insertion loss measured inside the passband is $IL = 3.7$ dB.

Apart from the insertion losses, the other measured characteristics are: center frequency $f_c = 3.671$ GHz, and bandwidth $BW = 117$ MHz. Overall, the measured response shows good agreement in terms of central frequency and filter bandwidth, as compared to the ideal design specifications. This is a clear indication that the relative permittivity of the ABSplus block is very close to the nominal value reported by the manufacturer ($\epsilon_r = 3.55$) [19]. On the contrary, the measured minimum return loss within the passband is worse ($RL = 12$ dB) than the expected value. In addition, we can clearly see that a number of reflection poles are not clearly visible. This means that the filter is not correctly tuned. In general, this behavior is normal with low accuracy manufacturing processes. The return loss is indeed the most sensitive parameter in the response of a microwave filter.

However, the detuning observed in the return loss response can be corrected by introducing tuning screws in the manufactured prototype, as shown in Fig. 8. In this case, standard $M3$

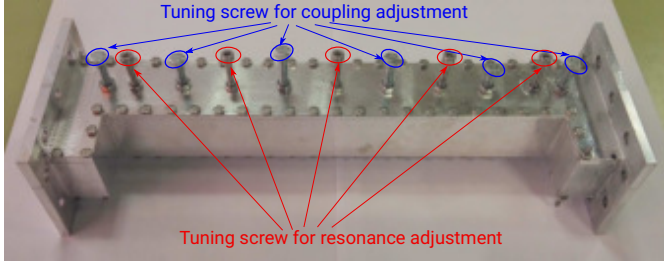


Fig. 8. Photograph of the manufactured filter based on air holes (Fig. 1(a)), after assembling. Details of the tuning screws used to compensate for manufacturing errors are also shown.

tuning screws were used. As we can see in the figure, a total of 11 tuning screws have been used for the fine tuning of the filter. Six screws are located in the center of the air holes, in order to adjust the couplings. Five more screws are placed in the middle of the resonators (between two contiguous air holes), to allow for the adjustment of the resonant frequencies of the individual resonators. For the installation of these last screws, the dielectric block has been perforated at the appropriate locations. In this context, it is interesting to note that the perforations will shift the resonances to higher frequencies. The presence of the screws in the resonators, however, will lower the resonant frequencies, thus compensating for the initial frequency shifts. This is the reason why the final prototype shown in Fig. 8 can be tuned, keeping the same center frequency as in the original structure without tuning screws.

The response of the hardware after tuning is also included in Fig. 7 (with square symbols). Results show that the tuning process was indeed effective. In particular, the filter has the same center frequency and bandwidth as for the initial specifications. Furthermore, an almost equiripple return loss response has been obtained with a $RL = 21$ dB. However, the improvements in the passband response come at the expense of a limited increase in the minimum insertion loss of the filter within the passband, which now increases to $IL = 3.9$ dB, as shown in the inset of Fig. 7. Overall, a good filter performance has been demonstrated with the manufactured prototype. Also, the tuning process has shown to be effective in compensating the manufacturing errors introduced by the 3D printing technique.

The second filter, based on dielectric posts, as shown in Fig. 1(b), has been manufactured using a similar strategy. Again, the metallic housing is manufactured from aluminum in two pieces, with a main body and a top cover, as shown in Fig. 9. In this case, an additional practical challenge is the alignment of the five elliptical dielectric resonators inside the empty evanescent waveguide section. To meet this challenge, in the 3D printing of the five dielectric resonators we have included two alignment pins of height p_h and diameter p_d , respectively, as shown in Fig. 10. Two holes per resonator are then drilled in the bottom wall of the main body, with slightly greater diameter than the alignment pins. The dielectric cylinders are then simply placed inside the metallic housing by introducing the pins in the corresponding holes. For practical

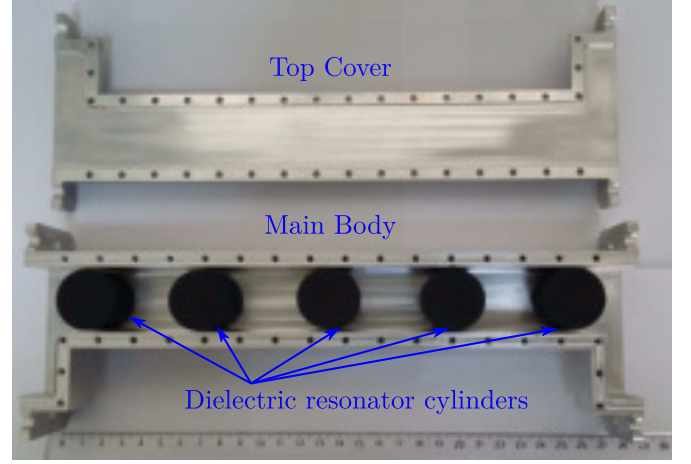


Fig. 9. Pieces of the manufactured filter with dielectric post resonators. The five dielectric elliptic cylinders are shown already mounted and aligned inside the empty evanescent waveguide section.

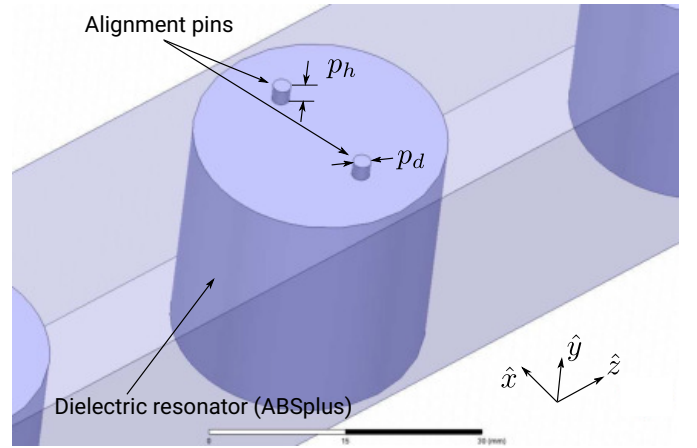


Fig. 10. Details of a dielectric cylinder resonator including the two pins incorporated for alignment inside the empty evanescent waveguide section. The alignment pins are placed along the \hat{x} -axis.

considerations related to the 3D printing process, the height and diameter of the pins were selected to be $p_h = 2$ mm and $p_d = 2$ mm, respectively. With these dimensions, we have verified with EM simulations that the pins do not have any significant influence on the electrical performance of the structure.

After assembling the dielectric cylinders, the measured scattering parameters of the filter are shown in Fig. 11. Comparison with respect to the simulated response is also shown, after including losses in the analysis of the structure. As we can see, the measured and simulated results show excellent agreement for both center frequency and bandwidth. The RL performance inside the passband without tuning is better in this case, with a minimum value of $RL = 18$ dB. The measured bandwidth at a constant return losses of 20 dB is 104 MHz. In addition, the measured minimum insertion loss within the passband is ($IL = 4.3$ dB) (see the inset of Fig. 11). This insertion loss is only 0.3 dB higher than the simulated response using $\tan \delta = 0.0053$ to model the ABSplus plastic, and the conductivity of aluminum for the

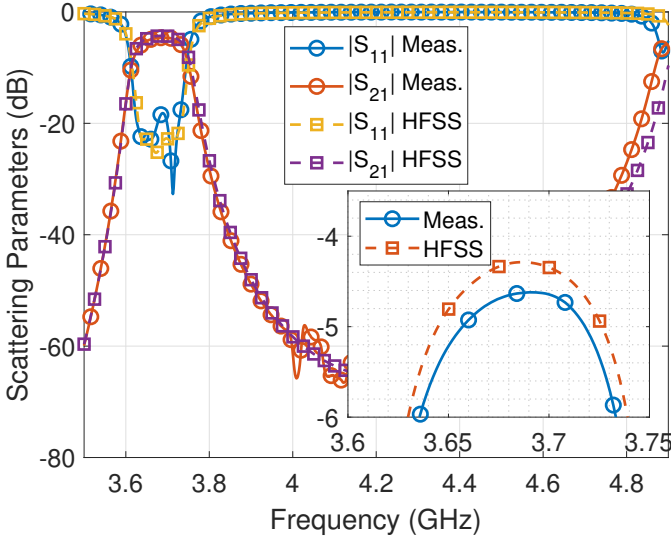


Fig. 11. Comparison between the measured and simulated S-parameters, for the dielectric posts filter. Simulations include losses in the dielectric resonators ($\tan \delta = 0.0053$) and finite conductivity in the housing ($\sigma = 3.8 \cdot 10^7$ S/m).

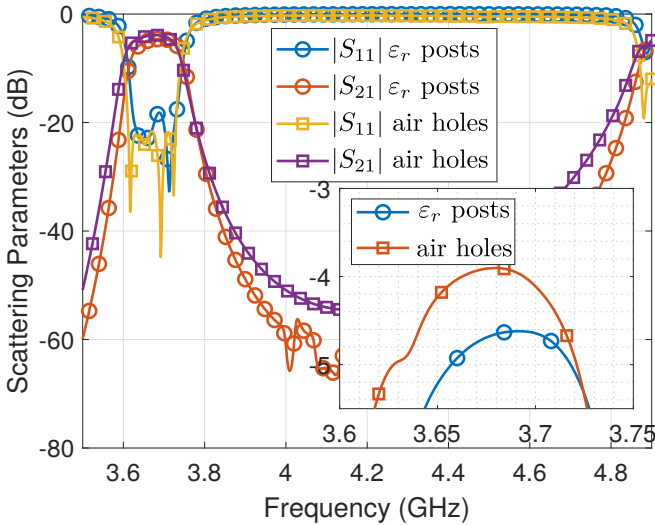


Fig. 12. Comparison between measured results of the two manufactured filters with $BW = 120$ MHz. Legend refers to Fig. 1(a) (air-holes) and Fig. 1(b) (ϵ_r -posts). The tuned response obtained with screws is used for comparison in the case of the air-holes filter.

housing. As it happened with the previous design, the loss tangent of the ABSplus plastic seems to be in the upper limit reported by the manufacturer ($0.0046 < \tan \delta < 0.0053$) [19]. Since in this case the agreement between measurements and simulations is good, we did not use any further post-manufacturing tuning mechanism.

Finally, in Fig. 12 we include a comparison between the measured responses obtained for the two filters that we have manufactured. The response of the air-hole filter used for this comparison is the one obtained after tuning with screws (see Fig. 8). Details of insertion losses can be observed in the inset of the figure. As shown, the filter based on air-holes has lower insertion losses ($IL = 3.9$ dB) as compared to the dielectric post filter ($IL = 4.3$ dB). This can be explained by the larger

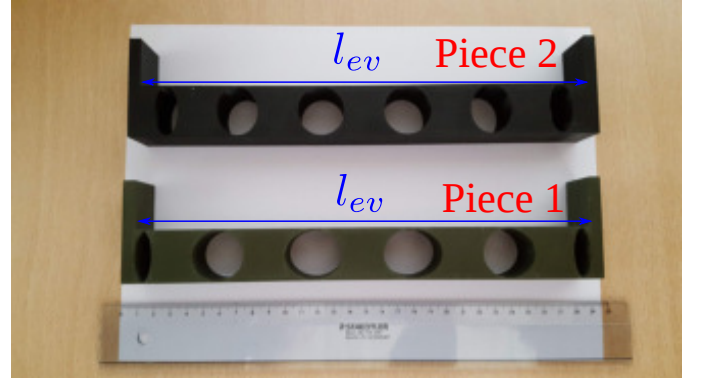


Fig. 13. Comparison of the dielectric pieces designed for the air-holes filters having different bandwidths. Shown at the bottom is the dielectric piece for the first filter with narrower bandwidth (Piece 1). Shown at the top is the dielectric piece for the new filter with wider bandwidth (Piece 2). Both pieces have the same length: $l_{ev} = 258.847$ mm.

dimension of this filter ($l_{tot} = 292.847$ mm) as compared to the dielectric post filter ($l_{tot} = 275.016$ mm). The extracted Q_U values from both filters are $Q_U = 305.75$ and $Q_U = 303.57$, respectively. This indicates that the solution based on air-holes leads to resonators of slightly higher Q_U , although at the expense of somewhat larger dimensions. Except for the insertion losses, the performances of the two filters are very similar, both inside and outside of the passband. In particular, both filters exhibit very similar measured *SFR* behaviors, with a first spurious band at about 4.9 GHz.

As a final study, we now show the capabilities of the hybrid manufacturing approach proposed in this work to produce different types of transfer functions without changing the filter housing. The idea is to use the same housing to generate different transfer functions by manufacturing new dielectric pieces with the 3D printer. To illustrate the basic idea, we now show the design of a new air-hole filter having the same specifications as before, except for the bandwidth which is increased to $BW = 175$ MHz.

For the design of this new filter, an important geometrical restriction must be taken into account, namely, that the total length (l_{ev}) for this second piece must be the same as the one of the first filter ($l_{ev} = 258.847$ mm). In Fig. 13 we show the dielectric piece of the previous design (Piece 1), and we compare it with the dielectric piece of the new design with increased bandwidth (Piece 2).

As we can see, the same length (l_{ev}) is preserved in both designs. The new dielectric piece (shown on top), however, has smaller air holes to allow for larger couplings. The smaller holes also increase the loading effects of the couplings into adjacent resonators. Consequently, the resonators become physically shorter, thus leading to air holes which are placed closer as compared to the first design (shown at the bottom). It is important to note that the total length (l_{ev}) can be made equal in both designs because of the additional degree of freedom provided by the length l_1 shown in Fig. 1(a) (distance between the step discontinuity and the first/last air-hole).

The design procedure for the filter with increased bandwidth is the same as previously described. The only difference is that

TABLE III
FINAL DIMENSIONS OF THE DESIGNED AIR-HOLES FILTER ACCORDING TO
FIG. 1(A), FOR $BW = 175$ MHz.

Var.	Value (mm)	Var.	Value (mm)	Var.	Value (mm)
l_{port}	10	l_1	8.25	r_1	6.752
l_d	7	l_2	22.059	r_2	11.702
l_{ev}	258.847	l_3	23.255	r_3	13.623
l_{tot}	292.847	l_4	23.411	r_x	14

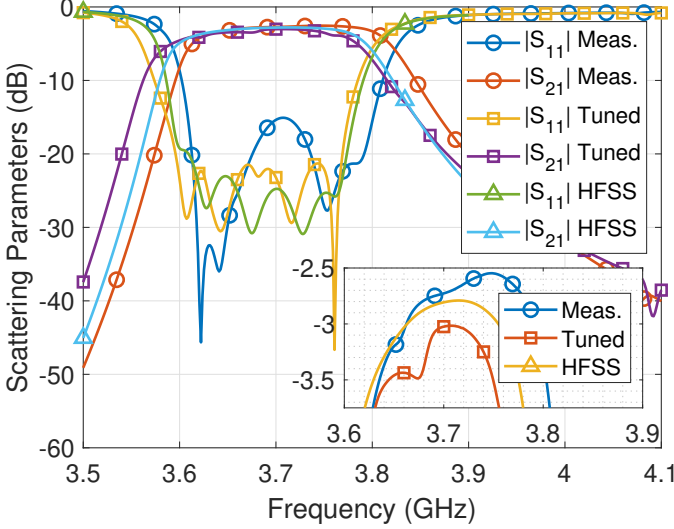


Fig. 14. Response of the air-holes filter designed with wider bandwidth ($BW = 175$ MHz). Measured results directly after manufacturing (circle symbols) are compared to results obtained after tuning (square symbols), and with simulated results obtained with the software tool HFSS (triangle symbols).

new coupling and Q_{ext} curves (similar to Fig. 2 and Fig. 3) are obtained using (3) and (4) with the new bandwidth (BW) specifications. The final dimensions for this filter, as defined in Fig. 1(a), are collected in Table III.

The new filter is obtained by replacing the dielectric Piece 1 with the dielectric Piece 2 inside the same metallic housing (shown in Fig. 6). The measured response obtained directly after manufacturing is shown in Fig. 14 (circle symbols).

In general, the performance obtained is quite good in terms of center frequency and bandwidth ($f_c = 3.71$ GHz, $BW = 180$ MHz). The minimum insertion loss inside the bandwidth is now lower due to the larger bandwidth ($IL = 2.5$ dB). In addition, the return losses are also good, being better than $RL = 15$ dB inside the useful bandwidth. In order to improve the return loss performance of the filter, we have also used similar tuning screws as previously described (see Fig. 8). The response obtained after tuning is also shown in Fig. 14 (square symbols). As we can see, after the tuning process we have a passband with a center frequency of $f_c = 3.687$ GHz, and a bandwidth of $BW = 172$ MHz. The measured results also show an almost equiripple response with return losses better than $RL = 21$ dB. These improvements in the passband again come at the expense of an increased insertion loss. The minimum insertion loss within the passband is $IL = 3$ dB. For comparison, the simulated response obtained with the software tool HFSS is also included in Fig. 14 (triangular symbols). For

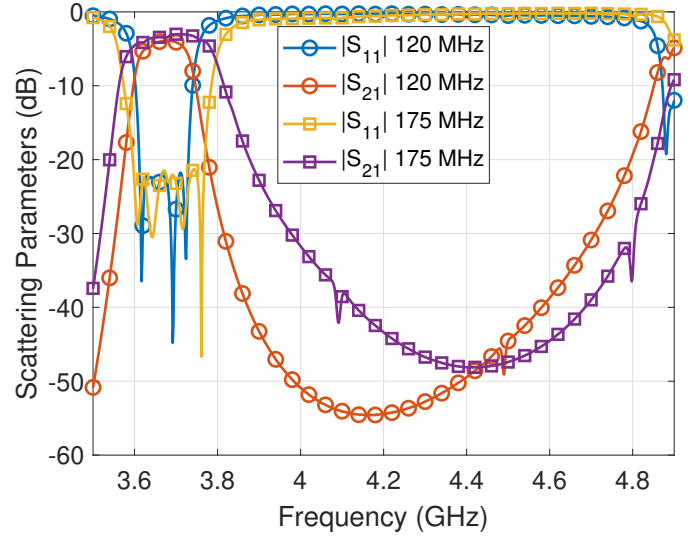


Fig. 15. Measured S-parameter responses of the two air-holes filters with different bandwidths. Responses are shown in a large frequency span to monitor the out of band performances.

this simulation the losses are characterized using the same parameters as described in the previous examples. As we can see, the losses predicted by the software tool are very similar to those measured directly after manufacturing, while the tuned prototype shows increased losses due to the effects of the tuning screws.

A final comparison between the two air-holes filters with different bandwidths is presented in Fig. 15. The measured responses after tuning have been selected for this comparison. We can clearly see the differences in bandwidth between the two filters. In both cases the return loss performance is very satisfactory (better than $RL = 20$ dB). The filter responses are shown in a large frequency span, so that the SFR performances can be observed. As we can clearly see, the first spurious band again appears at $f_{sp} \approx 4.8$ GHz for both filters, giving $SFR \approx 1$ GHz.

Overall, the results presented in this paper clearly show that the hybrid CNC milling and 3D printing manufacturing concept that we propose can be used to obtain flexible and low cost microwave filters with acceptable electrical performances. The only drawback is to have slightly higher values of insertion losses. However, we expect that this drawback may be eliminated once better quality 3D printing materials become commercially available.

IV. CONCLUSIONS

The main aim of this work is to show experimentally that the use of 3D-printed ABSplus as dielectric material for the design of evanescent bandpass filters at C-band is indeed viable. For this purpose, two filter structures using dielectrics and evanescent waveguide housings have been designed, manufactured and successfully measured. Both filters are based on an in-line topology, and combine low cost additive manufactured parts for the dielectrics with milled metallic parts for the external housing.

The first filter, based on air-holes, exhibits larger (Q_U) value as compared to a solution based on dielectric posts. However, the second option leads to more compact structures, and to the possibility of achieving higher bandwidths. The capability of implementing different transfer functions, by 3D printing several different dielectric pieces which are then integrated inside the same housing, has also been demonstrated. The measured electrical performances are satisfactory, but with slightly higher insertion losses due to the electrical properties of the employed ABSplus plastic. It is expected that improvements in insertion loss can be achieved as new 3D printing materials, with improved electrical properties, become commercially available.

From the results of this work, we conclude that the hybrid CNC milling and 3D printing manufacturing approach demonstrated in this paper is, indeed, a very valuable industrial tool for the rapid and flexible prototyping of practical microwave filters.

REFERENCES

- [1] V. Boria and B. Gimeno, "Waveguide filters for satellites," *IEEE Microw. Mag.*, pp. 60–70, October 2007.
- [2] R. J. Cameron, C. M. Kudsia, and R. R. Mansour, *Microwave Filters for Communication Systems: Fundamentals, Design and Applications*. John Wiley, Sons; Inc. Hoboken, New Jersey, 2018, 2nd ed.
- [3] X. Shang, M. Lancaster, and Y.-L. Dong, "W-band waveguide filter based on large TM120 resonators to ease CNC milling," *Electron. Lett.*, vol. 57, no. 7, pp. 488–490, March 2017.
- [4] M. D'Auria, W. J. Otter, B. T. W. Gillatt, C. Long-Collins, N. M. Ridler, and S. Lucyszyn, "3-D printed metal-pipe rectangular waveguides," *IEEE Trans. Compon. Packag. Manuf. Technol.*, vol. 5, no. 9, pp. 1339–1349, September 2015.
- [5] O. A. Peverini, M. Lumia, F. Calignano, G. Addamo, M. Lorusso, E. P. Ambrosio, D. Manfredi, and G. Virone, "Selective laser melting manufacturing of microwave waveguide devices," *IEEE Proc.*, vol. 105, no. 4, pp. 620–631, April 2017.
- [6] F. Calignano, D. Manfredi, E. P. Ambrosio, S. Biamino, M. Lombardi, E. Atzeni, A. Salmi, P. Minetola, L. Iuliano, and P. Fino, "Overview on additive manufacturing technologies," *IEEE Proc.*, vol. 105, no. 4, pp. 593–612, April 2017.
- [7] J. R. Montejó-Garai, I. O. Saracho-Pantoja, C. A. Leal-Sevillano, J. A. Ruiz-Cruz, and J. M. Rebollar, "Design of microwave waveguide devices for space and ground application implemented by additive manufacturing," in *2015 International Conference on Electromagnetics in Advanced Applications (ICEAA)*, Sep. 2015, pp. 325–328.
- [8] S. Khan, N. Vahabisani, and M. Daneshmand, "A fully 3-D printed waveguide and its application as microfluidically controlled waveguide switch," *IEEE Trans. Compon. Packag. Manuf. Technol.*, vol. 7, no. 1, pp. 70–80, January 2017.
- [9] K. Y. Chan, R. Ramer, and R. Sorrentino, "Low-cost ku-band waveguide devices using 3-D printing and liquid metal filling," *IEEE Trans. Microw. Theory Techn.*, vol. 66, no. 9, pp. 3993–4001, September 2018.
- [10] J. A. Lorente, M. M. Mendoza, A. Z. Petersson, L. Pambaguian, A. A. Melcon, and C. Ernst, "Single part microwave filters made from selective laser melting," in *Microwave Conference, 2009. EuMC 2009. European*, Sep. 2009, pp. 1421–1424.
- [11] C. Guo, X. Shang, J. Li, F. Zhang, M. J. Lancaster, and J. Xu, "A lightweight 3-D printed X-band bandpass filter based on spherical dual-mode resonators," *IEEE Microwave and Wireless Components Letters*, vol. 26, no. 8, pp. 568–570, Aug 2016.
- [12] C. Guo, X. Shang, M. J. Lancaster, and J. Xu, "A 3-D printed lightweight X-band waveguide filter based on spherical resonators," *IEEE Microwave and Wireless Components Letters*, vol. 25, no. 7, pp. 442–444, July 2015.
- [13] P. Booth and E. V. Lluich, "Enhancing the performance of waveguide filters using additive manufacturing," *IEEE Proc.*, vol. 105, no. 4, pp. 613–619, April 2017.
- [14] K. Salonitis, G. Tsoukantas, P. Stavropoulos, and A. Stournaras, *Virtual Modelling and Rapid Manufacturing - Advanced Research in Virtual and Rapid Prototyping*. CRC Press, Jan. 2003.
- [15] N.-H. Tran, V.-N. Nguyen, A.-V. Ngo, and V. Nguyen, "Study on the effect of fused deposition modeling (FDM) process parameters on the printed part quality," *Int. Journal of Engineering Research and Application*, vol. 7, no. 12, pp. 71–77, December 2017.
- [16] C. Carceller, F. Gentili, D. Reichartzeder, W. Bschi, and M. Schwentenwein, "Practical considerations in the design of monoblock TM dielectric resonator filters with additive manufacturing," in *2017 International Conference on Electromagnetics in Advanced Applications (ICEAA)*, Sep. 2017, pp. 364–367.
- [17] Y. Marchives, N. Delhote, S. Verdeyme, and P. M. Iglesias, "Wide-band dielectric filter at C-band manufactured by stereolithography," in *Microwave Conference (EuMC), 2014 44th European*, Oct. 2014, pp. 187–190.
- [18] A. Perigaud, O. Tantot, N. Delhote, S. Verdeyme, S. Bila, and D. Bailargeat, "Bandpass filter based on skeleton-like monoblock dielectric pucks made by additive manufacturing," in *2018 48th European Microwave Conference (EuMC)*, Sep. 2018, pp. 296–299.
- [19] Stratasys. (2016, August) Absplus datasheet. [Online]. Available: http://usglobalimages.stratasys.com/Main/Files/Material_Spec_Sheets/MSS_FDM_ABSplusP430.pdf
- [20] A. Pons-Abenza, A. Alvarez-Melcon, F. D. Quesada-Pereira, and L. Arche-Andradas, "Frequency correction design technique for additive manufactured cavity filters," in *2018 48th European Microwave Conference (EuMC)*, Sep. 2018, pp. 288–291.
- [21] G. Matthaei, L. Young, and E. Yones, *Microwave Filters, Impedance Matching Networks, and Coupling Structures*. Boston, Massachusetts, USA: Artech House, 1980.
- [22] ANSYS, "HFSS version 19.2," <https://www.ansys.com/products/electronics/ansys-electronics-desktop>, 2019.
- [23] Stratasys. (2017, May) Dimension 1200es 3D printer. [Online]. Available: <http://www.stratasys.com/es/impresoras-3d/design-series/dimension-1200es>